

M. Lehnert, G. Arnoux, S. Brezinsek, J. Flanagan, S.N. Gerasimov,
N. Hartmann, T.C. Hender, A. Huber, S. Jachmich, V. Kiptily, U. Kruezi,
G.F. Matthews, J. Morris, V.V. Plyusnin, C. Reux, V. Riccardo, B. Sieglin,
P.C. de Vries and JET EFDA contributors

Impact and Mitigation of Disruptions with the ITER-Like Wall in JET

“This document is intended for publication in the open literature. It is made available on the understanding that it may not be further circulated and extracts or references may not be published prior to publication of the original when applicable, or without the consent of the Publications Officer, EFDA, Culham Science Centre, Abingdon, Oxon, OX14 3DB, UK.”

“Enquiries about Copyright and reproduction should be addressed to the Publications Officer, EFDA, Culham Science Centre, Abingdon, Oxon, OX14 3DB, UK.”

The contents of this preprint and all other JET EFDA Preprints and Conference Papers are available to view online free at www.iop.org/Jet. This site has full search facilities and e-mail alert options. The diagrams contained within the PDFs on this site are hyperlinked from the year 1996 onwards.

Impact and Mitigation of Disruptions with the ITER-Like Wall in JET

M. Lehnen¹, G. Arnoux², S. Brezinsek¹, J. Flanagan², S.N. Gerasimov²,
N. Hartmann¹, T.C. Hender², A. Huber¹, S. Jachmich³, V. Kiptily², U. Kruezi²,
G.F. Matthews², J. Morris², V.V. Plyusnin⁴, C. Reux⁵, V. Riccardo², B. Sieglin⁶,
P.C. de Vries⁷ and JET EFDA contributors*

JET-EFDA, Culham Science Centre, OX14 3DB, Abingdon, UK

¹*Plasma Physics, Forschungszentrum Jülich, Association EURATOM-FZJ, Trilateral Euregio Cluster,
52425 Jülich, Germany*

²*EURATOM-CCFE Fusion Association, Culham Science Centre, OX14 3DB, Abingdon, OXON, UK*

³*Laboratoire de Physique des Plasmas-Laboratorium voor Plasmafysica, Association EURATOM
Belgian State, ERM/KMS, B-1000 Brussels, Belgium*

⁴*Instituto de Plasmas e Fusão Nuclear/IST, Associação EURATOM-IST, Av. Rovisco Pais, 1049-001 Lisbon, Portugal*

⁵*Ecole Polytechnique, LPP, CNRS UMR 7648, 91128 Palaiseau, France*

⁶*Max-Planck-Institut für Plasmaphysik, EURATOM-Assoziation, D-85748 Garching,*

** See annex of F. Romanelli et al, "Overview of JET Results",
(24th IAEA Fusion Energy Conference, San Diego, USA (2012)).*

ABSTRACT

Disruptions are a critical issue for ITER because of the high thermal and magnetic energies that are released on short time scales, which results in extreme forces and heat loads. The choice of material of the plasma facing components (PFCs) can have significant impact on the loads that arise during a disruption. With the ITER-like wall (ILW) in JET made of beryllium in the main chamber and tungsten in the divertor, the main finding is a low fraction of radiation. This has dropped significantly with the ILW from 50–100% of the total energy being dissipated during disruptions in CFC wall plasmas, to less than 50% on average and down to just 10% for VDEs. All other changes in disruption properties and loads are consequences of this low radiation: long current quenches, high vessel forces caused by halo currents and toroidal current asymmetries as well as severe heat loads. Temperatures close to the melting limit have been locally observed on upper first wall structures during deliberate VDE and even at plasma currents as low as 1.5MA and thermal energy of about 1.5MJ only. A high radiation fraction can be regained by massive injection of a mixture of 10%Ar with 90%D₂. This accelerates the current quench thus reducing the halo current and sideways impulse. The temperature of PFCs stays below 400°C. MGI is now a mandatory tool to mitigate disruptions in closed-loop operation for currents at and above 2.5MA in JET.

1. INTRODUCTION

Disruptions are a critical issue for ITER because of the high thermal and magnetic energies that are released on short time scales, which results in extreme forces and heat loads being capable of damaging plasma facing components (PFCs) [1]. The new wall in JET with its main chamber material beryllium and the divertor made of tungsten [2] is a unique test bed to study disruptions under ITER-like conditions. Indeed, as it is shown in this paper, the material of the plasma-facing components has significant impact on the disruption properties and related loads. But the wall material does not only affect the disruption properties, it also changes plasma performance and requires therefore adjustment of plasma control in order to avoid disruptions. Enhanced core radiation by sputtered tungsten is one of the new issues to be addressed by proper control of divertor temperature to prevent a radiative collapse. Also density control has changed with the ITER-like wall (ILW), requiring more gas feeding to achieve sufficient density to avoid locked error field modes. The density limit itself has changed as well. Not only the H- to L-mode back transition occurs at higher densities, but also the dynamics of the density limit disruption are slowed down, giving more time to react and to prevent from disruptions. Most of these new control issues causing disruptions in the early phase of the ILW have been solved during the campaigns in 2011/2012. Disruptions also impact on machine conditioning by creating or mobilising dust and by loading PFCs with deuterium and impurities. This had significant impact on the breakdown and performance of subsequent pulses with carbon wall, but has become negligible with the ILW. These disruption related topics are discussed in more detail in [3, 4].

This paper will mainly focus on the disruption itself, namely its properties, resulting loads

and their mitigation. The data presented are disruptions in the pulse interval 65000–79853 for CFC, which is data with the same divertor configuration as for the ILW and 80130–83482 for the ILW, which corresponds to the first ILW campaigns in 2011/2012. This database contains both, unintentional disruptions and those done deliberately in dedicated experiments. Disruptions with massive gas injection are included in this database, but will be analysed separately from the rest of the data. The paper is structured in three parts. The first part will discuss the disruption properties (section 2), which focusses on the energy dissipation and the resulting timescales. The disruption loads including electro-magnetic and thermal loads as well as the generation of runaways will be addressed in part two (section 3). Finally, part three (section 4) analyses disruption mitigation by means of massive gas injection.

2. DISRUPTION PROPERTIES

The most important difference between the ILW and PFCs made of carbon is the absence of radiating impurities during the disruption process. This has significant implications: a) low radiation during the current quench phase, b) a hot current quench plasma, c) long current decay times, d) high heat loads caused by conduction of magnetic energy to PFCs, e) higher impact on the vacuum vessel by halo currents and current asymmetries. Figure 1 shows in a nutshell the typical characteristics for two representative disruptions, one with CFC wall and the other with the ILW. For the ILW the current quench (CQ) lasts for about 50ms. The radiation is low and peaks at about 50MW but is much lower for most of the CQ. The electron temperature is high at around 200eV for the initial CQ before significant vertical plasma movement occurs. The upward displacement is slow and the halo current stays high for several 10 ms. The CQ with CFC is much faster, about 28ms, and the radiation peaks at 490 MW but staying high throughout the early CQ. The electron temperature is low and cannot be detected by the ECE diagnostic. The vertical movement is fast and although the halo current peaks at the same level as for the ILW, the halo current phase is much shorter. In the following, we will discuss the changes in the disruption properties in more detail in this section, focussing on energy loss mechanisms and related timescales. The resulting electro-magnetic and thermal loads are discussed in the next section.

2.1. RADIATION AND ENERGY BALANCE

The total stored energy in the plasma, consisting of magnetic energy W_{mag} and thermal energy W_{th} , is dissipated during a disruption through up to four loss channels. It can be radiated (W_{rad}), coupled into vessel and poloidal field coils (W_{coupled}), conducted to PFCs (W_{cond}) or partly converted to runaway electrons (W_{RE}):

$$W_{\text{th}} + W_{\text{mag}} = W_{\text{rad}} + W_{\text{coupled}} + W_{\text{cond}} + W_{\text{RE}} \quad (1)$$

The coupled energy is calculated from the current decay using a lumped parameter model for the

mutual inductance, which includes energy flow between plasma, vacuum vessel, divertor and poloidal field coils [5, 6]. The model does not account for changes in the inductances caused by vertical displacement and shrinking of the plasma cross-section, which can lead to a larger error for vertical displacement events (VDEs). An example of the currents calculated by the model is given in figure 2. The vessel current is determined by subtracting the plasma current measured by in-vessel coils from the current measured by a Rogowski coil situated outside the vessel. The vessel current and the divertor current compares well to the calculated currents until most of the magnetic energy is dissipated. In the late phase of the CQ, measured and calculated currents deviate, which might be related to plasma displacement and to the missing divertor power supply in the model. However, this deviation affects the calculated energy only marginally.

Figure 3 shows the energy coupled into the vacuum vessel and the total energy being dissipated in external structures as function of the current decay time. The latter is taken as the linear current decay time extrapolated from the drop in current from 80% to 20% of the pre-TQ value. This definition of the CQ time is used throughout the paper, except otherwise stated. The resistive time of the vacuum vessel is about 2.9 ms and therefore the energy coupled into the vessel drops with increasing current quench time. The maximum energy dissipated in the vessel is about 30% of the magnetic energy for the fastest current quenches with about 10 ms duration. The divertor and poloidal field coils have a time constant of about 1s. Therefore, the total energy coupled is decaying slower with τ_{CQ} and ranges between about 55% for fast CQs and 40% for slow CQs with several 100ms duration. The fraction of magnetic energy being stored outside the plasma is 65%, which would be the upper limit for what can be coupled into the structure.

The energy that is dissipated in the plasma is given by $W_{\text{plasma}} = W_{\text{th}} + W_{\text{mag}} - W_{\text{coupled}}$. Figure 4 compares the energy being radiated during the entire disruption as measured by bolometry with W_{plasma} . Most of the data points with CFC wall are above 50% radiation fraction, whereas with the ILW radiation is mainly below 50%. Lowest radiation fractions of about 10% are found during pre-TQ VDEs. The issue of VDEs will be discussed again and some definitions should be given here. A vertical displacement can occur intentionally or unintentionally before the thermal quench (pre-TQ VDE) with significant displacement of the plasma column at the time of the TQ. This is usually in the literature referred to as a VDE. However, disruptions can also develop a vertical displacement after the TQ occurred and in order to distinguish both types of VDEs, this will be called a post-TQ VDE in the discussion of disruption loads later on. The acronym VDE will cover in the following both types, pre-TQ and post-TQ VDEs.

A closer look on the statistical distribution of the radiation fraction is given in figure 5 distinguishing between pre-TQ VDEs and all other disruptions. In the example of figure 1, we have seen that with the ILW, the radiated power is low during the entire disruption. Therefore, the energy loss by radiation can take much longer compared to vertical growth times. As a consequence, pre-TQ VDEs with the ILW have a significantly lower fraction of radiated energy compared to other disruptions. Also for CFC experiments, these VDEs tend to have lower radiation fractions than

natural unmitigated disruptions, but the difference is less pronounced due to the high radiated power. The impurities that radiate during the current quench are mainly released during the thermal quench (TQ). It has been shown that especially the heat flux into the inner divertor plays a significant role on releasing carbon from deposited layers [7]. Strong layer formation is absent with the ILW. Dust being mobilised or created during the disruption has been measured by the high resolution Thomson scattering diagnostic (HRTS) in JET, which records the light emission from dust particles being hit by the intense laser beam [8]. With the ILW, the amount of detected dust is reduced by a factor 10 to 100 compared to CFC [3]. The low amount of released or mobilised particles together with the low radiation efficiency of beryllium is in agreement with the strong reduction in radiation.

2.2 TIMESCALES

Important for the mechanical but also thermal loads is the timescale of the current quench. Figure 6a compares the statistics of the CQ times with ILW and with CFC. The CQ duration is given as the extrapolated linear current decay time (see definition for figure 3). Here, the CQ time is normalised to the area of the plasma cross-section in order to compare with other tokamaks with similar aspect ratio [9]. Disruptions with significant runaway current are excluded, i.e. the neutron count within the 80%-20% time interval is limited to 1012. The distribution for CFC peaks at about 3ms/m^2 , whereas the distribution is much broader and clearly shifted to longer CQ times for the ILW. A substantial fraction of about 35% of the disruptions with ILW has decay times with more than 20ms/m^2 .

Figure 6b shows the same set of data, but now restricted to disruptions which are vertically stable, i.e. with a vertical movement below 0.25m by the time 50% of I_p is reached. With this limitation, we exclude plasma movement as reason for the current decay. Still, most of the CFC disruptions have a fast current decay, but all the ILW disruptions in the subset have a CQ duration longer than 20ms/m^2 with only one exception. This outlier is caused by a failure in radial position control, causing the plasma to be moved into the inner poloidal limiter. The resulting CQ time is 10.5ms/m^2 . Thus, with the ILW fast current quenches can only be observed in disruptions with a vertical or radial displacement of the plasma column.

2.3 POWER BALANCE DURING THE CURRENT QUENCH

The energy dissipation in the current quench is governed by the following power balance:

$$\frac{d}{dt} W_{\text{mag}} = -P_{\text{coupled}} - P_{\text{ohmic}} \quad (2a)$$

$$\frac{d}{dt} W_{\text{th}} = P_{\text{ohmic}} - P_{\text{rad}} - P_{\text{cond}} \quad (2b)$$

The magnetic energy is dissipated by inductive coupling and ohmic heating, energy transfer to runaway electrons is not considered here. The thermal energy is governed by the balance between ohmic heating and radiation. For most of the disruptions with CFC wall, the radiated power P_{rad} balances the ohmic heating P_{ohmic} , the thermal energy and plasma temperature remain low and

the current quench time is short. When P_{rad} becomes comparable to the conductive loss P_{cond} , the characteristic time for thermal transport starts to play a role. Thus, for low radiation fractions as seen with the ILW, the thermal energy - and therefore the plasma temperature - will rise until P_{cond} balances $P_{\text{ohmic}} - P_{\text{rad}}$. A consequence of the higher temperature is a longer current decay.

Figure 7 summarises the dependence of the radiated energy fraction on the current quench time. Except those marked as VDE, all data points correspond to disruptions without significant vertical movement during the current quench. Thus, the CQ time depends only on the loss rate either by radiation or by transport. As discussed above, if the radiated power - and therefore the radiation fraction - is high, the current quench time is determined by the energy loss through radiation: τ_{rad} . This is the case for disruptions with CFC. With the ILW, the radiation fraction drops and transport, namely conduction (τ_{cond}), determines the CQ time. During VDEs, the current quench is faster because of the vertical movement with characteristic time τ_{vertical} , which increases P_{cond} .

The equations 2 can be solved using the following expressions:

$$P_{\text{coupled}} = I_P \frac{d}{dt} (\underline{M}_P \cdot \underline{I}_S) \approx I_P \underline{M}_P \cdot \frac{d}{dt} \underline{I}_S \quad (3a)$$

$$P_{\text{ohmic}} = 2\pi R \eta I_P^2 / S \quad (3b)$$

$$P_{\text{rad}} = 2\pi R S n_e^2 L_Z / Z_e \quad (3c)$$

$$P_{\text{cond}} = W_{\text{th}} / \tau_{\text{cond}} \quad (3d)$$

$$W_{\text{mag}} = 0.5 L_P I_P^2 \quad (3e)$$

$$W_{\text{th}} = 2k T_e n_e 2\pi R S \quad (3f)$$

$$\underline{M}_S \frac{d}{dt} \underline{I}_S = \underline{R}_S \underline{I}_S \quad (3g)$$

with major radius R , plasma cross-section area S , inductance of the plasma L_P , mutual inductance between plasma and structure elements \underline{M}_P , inductance matrix for structure elements \underline{M}_S , resistance of the structure elements \underline{R}_S , Spitzer resistivity η and cooling rate L_Z . The latter is taken from corona equilibrium assuming impurity influx takes place only during the thermal quench. The inductances matrices are taken from the same model that has been used for the estimation of the coupled energy (section 2.1). As mentioned before, this simplified model does not take into account changes in the plasma cross-section or vertical displacements, i.e. $d\underline{M}_P/dt = 0$ is assumed. It is therefore not suitable to describe VDEs. Substituting eqs.3 into eqs.2 gives a solution for the current in the plasma I_P and in the structure elements \underline{I}_S and for the electron temperature T_e . The plasma density n_e is determined by the impurity density, which is input to the model.

Figure 8 shows two cases calculated with the above model: injection of Be for the ILW case and injection of C for the CFC case. The impurity density is $n_Z = 7 \times 10^{18} \text{ m}^{-3}$ in both examples. The thermal loss time is set to $\tau_{\text{cond}} = 30 \text{ ms}$. The initial current is 2.0MA and the initial electron temperature is set to 5eV. Due to the high cooling rate of carbon, radiation dominates the CFC case. This results in a fast current quench with $\tau_{\text{CQ}}/S = 3.5 \text{ ms/m}^2$ and a radiation fraction of $W_{\text{rad}}/(W_{\text{mag}} - W_{\text{coupled}}) = 1.0$. For Be injection, a fast rise of the electron temperature is seen (logarithmic time axis!), because of the low cooling rate of Be and the low radiated power, which cannot compensate the ohmic heating. The temperature rises to about 100eV until Pcond is sufficiently high to compensate ohmic. Because of the high T_e , the CQ is slow with $\tau_{\text{CQ}}/S = 140 \text{ ms/m}^2$ and the radiation fraction is low $W_{\text{rad}}/(W_{\text{mag}} - W_{\text{coupled}}) = 0.45$. The calculated radiation fractions and CQ times represent well the experimental findings (see figure 7).

In inter-machine comparisons, the current decay time is often plotted versus plasma current density. In order to extrapolate to ITER it is important to distinguish between the causes for the current decay. Vertical growth times for example can differ from tokamak to tokamak and are especially in ITER expected to be long. Figure 9 shows the current decay time discussed before as function of the pre-TQ current. As shown earlier, the lower limit of τ_{CQ}/S is determined by vertical displacement during the CQ (pre-TQ VDEs are excluded). The lower limit for CFC is given by radiation and the highest carbon density can be calculated according to the simple model described above, which gives $n_C \approx 1.5 \times 10^{19} \text{ m}^{-3}$ as an upper boundary. According to the model, τ_{CQ} increases with plasma current, because the ohmic heating increases with I^2P but is partly compensated by a strong temperature dependence of LC - and therefore Prad - for temperatures of a few eV .

It is important to mention that within this data set discussed here, thermal energies at the time of the TQ were low and could not cause melting of tungsten in the divertor. Therefore, tungsten influx is assumed to be low and accordingly radiation caused by tungsten is low. The situation might change, if tungsten is released by melting events during the TQ.

3 DISRUPTION LOADS

3.1 ELECTRO-MAGNETIC LOADS

Vertical forces on the vacuum vessel can arise by eddy currents and poloidal halo currents. Additionally, $m = n = 1$ kink modes during the current quench result in sideways forces [10]. The amplitude of the halo current depends on the vertical stability of the CQ plasma: the vertical growth time is in competition to the current decay rate. If the decay rate is higher than the vertical growth rate, vertical displacement is limited during the CQ. This is the recipe followed with massive gas injection in order to reduce halo currents. On the other hand, a high current quench rate acts destabilising and accelerates the vertical displacement. In order to quantify the competition between CQ rate and vertical growth rate, we have chosen to represent the vertical growth time by the time $\tau_v^{0.3}$ from the current spike to a displacement of 0.3m. This is compared in figure 10 to the time τ_{CQ}^{70} needed for a reduction in plasma current to 70% of the pre-TQ current I_0^P . Disruptions with a

vertical displacement below 0.3m at 70% IOP are shown with open symbols. Closed symbols refer to disruptions with a higher vertical displacement. When the CQ rate is very high or the vertical movement is very slow, the displacement of the plasma column can be less than 0.3m for the entire CQ and $\tau_v^{0.3}$ is infinity. These data points are plotted in the grey region. Three cases are shown, disruptions with x-point for low and high triangularity and disruptions in limiter configuration. For all cases, a clear increase of the vertical growth time with CQ time is seen. Towards very short CQ times, the vertical growth rate saturates and the vertical displacement is limited by the CQ time. This is seen for disruptions with CFC wall. Stability is also reached for very long CQ times, when the external poloidal field can follow the changes in plasma current. This stability regime is established for the slow current quenches with the ILW.

Because of the fast vertical growth time with high triangularity, the fraction of vertically stable current quenches with CFC is low. With decreasing δ , the minimum in $\tau_v^{0.3}$ increases and more disruptions with CFC become vertically stable during the CQ. The ILW data points extend towards slow CQs and vertically stable CQs are found for $\tau_v^{0.3}$ above about 100ms, where $\tau_v^{0.3}$ becomes larger than τ_{CQ}^{70} . The window in τ_{CQ}^{70} with vertically unstable current quenches lies between the minimum $\tau_v^{0.3}$ and about 100 ms. This window is shrinking with lower shaping. Interestingly, for the ILW, most of the data points lie in this time window. Therefore and in contrast to CFC, limiter disruptions with ILW are prone to post-TQ vertical displacements. This can be seen in figure 11: for high triangularity almost no change in distribution for the vertical displacement at 70% I_0^P is seen, whereas with lower triangularity and, more pronounced, for limiter pulses the probability for vertical displacement increases. Thus, especially for low triangularity and limiter configurations an increase of the peak halo current is seen with ILW.

As stated above, the maximum poloidal halo current measured in the structure of the upper dump plates depends on the competition between current decay and vertical displacement. To quantify this competition, we take the ratio $\xi_\tau \stackrel{70}{=} \tau_{CQ} / \tau^{0.3}$, which is from the experimental point of view easy to determine. The maximum halo current for post-TQ VDEs with upward movement during the CQ is shown in figure 12 as function of ξ_τ . The halo current is low but finite for $\xi_\tau < 1$ and increases quickly when $\xi_\tau > 1$. This behaviour is well described by a simple halo model (see [11] and appendix A). In the case of $\xi_\tau < 1$, plasma core current is induced in the halo, but "convection" of current into the halo region is negligible. Because of the fast current decay, the safety factor q_H will increase during the CQ resulting in a small poloidal halo current fraction. For $\xi_\tau > 1$ toroidal and poloidal halo current increases as the core area starts to decrease, which leads to transfer of current into the halo region and change in toroidal flux. Eventually with further increasing ξ_τ , the safety factor will drop during the CQ and the poloidal halo current will become equal to the toroidal halo current. In the experiment, the upward movement is slowed down during the CQ and eventually reversed in the late CQ. This prevents further decrease of q_H and limits therefore the increase in $I_{H,pol}$ with increasing ξ_τ in contrast to the model.

With respect to the impact of halo currents on the vessel, not only the maximum of I_H/I_P is

relevant, but also the time for which the force is applied. Figure 13 summarize the above findings. It shows I_H/I_P as function of the linear current quench time as defined in section 2.2. As expected from the above discussion, the halo current remains low for slow vertical movement and increases up to around $I_H/I_P = 0.2$ for the non-VDE cases shown. Higher fraction with up to $I_H/I_P = 0.4$ are seen for VDEs. Both, ILW and C wall, reach the same maximum value, but for different durations of the CQ. This has important consequence on the duration of the halo current phase and the resulting displacement of the vessel as described in [3] and shown in the following.

In order to account for the duration and the amplitude with which the force to the vessel is applied, the vessel displacement is given in figure 14 as function of the impulse from symmetric halo currents i_{vertical} and from current asymmetries i_{sideways} :

$$i_{\text{vertical}} = B_t \int_{\text{CQ}} \langle I_H \rangle dt \quad (4a)$$

$$i_{\text{sideways}} = \frac{\pi}{2} B_t \max \left(\left\| \int_{\text{CQ}} \Delta \underline{M}_{iz} dt \right\| \right), \quad (4b)$$

with the averaged poloidal halo current $\langle I_H \rangle$ and the asymmetry in the vertical moment of the plasma current $\Delta M_{iz} = (M_{iz}^5 - M_{iz}^1, M_{iz}^7 - M_{iz}^3)$. The vertical moment is measured at four toroidal locations (octants 1,3,5,7) [10]. Because the vessel is mechanically held at the end of the top and bottom main vertical ports during plasma operation a vertical force results in a rolling motion, whereas toroidal asymmetries in the halo currents lead to sideways displacements of the vessel (see schematic in figure 14). The vessel roll is caused not only by halo currents, but also by eddy currents. Therefore, figure 14a shows the total amplitude of the vessel roll, being related to forces from both currents and the positive amplitude of the vessel roll only, being related mainly to the impact of the halo current. The offset between both sets of data is due to eddy currents. The positive vessel roll increases steadily with the halo current impulse. Like for a spring-mass system, saturation would be expected for halo current durations longer than half of the resonance period of the vessel. The resonance frequency is about 14Hz and the saturation is therefore expected at about 35ms. As seen from figure 13, the halo current fraction for the ILW peaks at current quench times of this order. Therefore, an increase of vessel displacement due to the longer halo current phase with ILW is seen and already at still moderate plasma current the vessel displacements are close to the limits defined for JET to keep the risk of leakage acceptable. The positive vessel roll follows the amplitude calculated for a spring-mass system with maximum applied force of 1.2MN (corresponding to $B_t = 3\text{T}$, $I_P = 2\text{MA}$ and $I_H/I_P = 0.2$), a mass of 160t and resonant frequency of 14Hz. The impact from current asymmetries depends on their amplitude and on the rotation frequency of the $m = n = 1$ kink mode. If not close to the resonant frequency, a rotating mode can cause less sideways displacement than a stationary mode. Therefore, i_{sideways} is taken as the maximum directional impulse during the CQ (eq.4). A linear increase of the sideways displacement with i_{sideways} is found, showing highest displacements for the

ILW. The linear dependence indicates that for this dataset, resonant amplification is not significant. However, resonant amplification remains an open issue for ITER as the physics understanding for the rotation is not yet established, which makes predictions for ITER uncertain.

3.2 THERMAL LOADS

Severe heat loads have been observed with the ILW during the current quench because of the lack of radiating impurities [7]. Looking again at equations 2, we find if P_{rad} is sufficiently low, the thermal energy will increase to a level depending on the loss time by conduction or convection τ_{cond} and P_{cond} will compensate P_{ohmic} . The energy being conducted (or convected) to PFC, W_{cond} , is calculated from the energy balance (eq.1). This energy is on average higher for the ILW compared to CFC. However, the heat load impact, namely the temperature rise on PFCs, depends not only on the energy, but also on the deposition duration and the wetted area. Figure 15 shows W_{cond} as function of the characteristic loss time of the magnetic energy, $\tau_{\text{mag}} = 0.5 - \tau_{\text{CQ}}$, which gives an upper limit of the heat deposition time. Disruptions with CFC tend towards low W_{cond} and short τ_{mag} . With the ILW, W_{cond} can be very high. As long as τ_{mag} is sufficiently long, the temperature rise can be expected to be low. However, for those disruptions experiencing vertical displacement during the CQ, the deposition time can be short whilst W_{cond} is high. Beside post-TQ VDEs, this is especially the case for pre-TQ VDEs as they show the lowest level of radiation. Such disruptions have the potential to cause localised melting of the Be PFCs at the upper wall protection of JET as it was observed by in-vessel video inspection. During the CQ of these disruptions, one or more temperature peaks are observed with the IR camera. Figure 15b shows the maximum temperature rise during these events, which is clearly correlated to $W_{\text{cond}} \times \tau_{\text{mag}}^{-1/2}$. But it has to be kept in mind that this ΔT does not necessarily directly reflect the energy being deposited. The dashed red line indicates the average correlation, resulting in a wetted area of 3 m^2 , the black dashed line is the most severe envelope of the data with $A_{\text{wetted}} = 1.75 \text{ m}^2$. Further analysis of IR data is necessary to directly estimate the wetted area. Any movement of the plasma contact point during the CQ would affect A_{wetted} and could even lead to a beneficial spreading of the power load. Additionally, as mention above, τ_{mag} is only an upper limit for the deposition time. It can be significantly shorter, when for example instabilities during the CQ cause a fast loss of thermal energy being stored in the current quench plasma.

3.3 RUNAWAYS

Runaway electron (RE) formation has not yet been seen so far in disruptions with the ILW [12], which is contrast to the experience with the previous CFC wall, where about 15% of the disruptions in x-point configuration developed runaway electrons [13]. Assuming that the Dreicer mechanism is the main driver for runaway generation in JET, electron densities and temperatures during the current quench have a strong impact on whether RE are generated or not. We will use a simple picture to illustrate the situation. RE formation is expected if E/ED is about larger than 0.01, where ED is

the Dreicer field (see [14] for a comprehensive summary). The electric field scales with electron temperature (Spitzer resistivity) and plasma current like $E \sim I_p^1 T_e^{-1.5}$. This gives a scaling for the ratio of the fields of $E/E_D \sim I_p^1 n^{-1} T_e^{-0.5}$. Both, higher temperature and higher density will lead to a decrease in E/E_D for constant plasma current. The rise in electron density depends to first order on the impurity influx, i.e. impurity density. For the same impurity density (carbon for CFC and beryllium for ILW), n_e will be of the same order, but T_e will be about an order of magnitude higher [7], causing a smaller E/E_D compared to CFC. On the other hand, for the same T_e for both, CFC and ILW, the impurity density has to be about 20 times higher for the ILW and E/E_D will be smaller for the ILW as well. In addition to the impact of the plasma parameter on the generation mechanism, losses could play a significant role with the ILW as enhanced MHD is more frequently observed for slow current quenches. It is interesting to note that a slowing down of the current quench had already been observed, when JET was operated with Be limiter [15]. During this operation period, RE were not observed as now with the ILW.

A reliable recipe to generate runaways in a disruption with CFC wall was the injection of argon through a standard gas inlet into a limiter plasma at high magnetic field. An exact repeat of a reference pulse at 3T and 2.0MA with about 0.6MA of runaway current has been tried with the ILW wall, showing no signs of runaway formation. The maximum current decay rate was 45MA/s only for 5.3×10^{20} injected Ar atoms, whereas with CFC the rate was three times higher, 145MA/s with 6.6×10^{20} Ar atoms. This can be attributed to carbon release which adds to the radiation from the injected argon and accelerates the CQ further. The repeat with the ILW showed in addition strong magnetic fluctuation, which are known to cause prompt loss of high energy particles.

4. MITIGATION BY MASSIVE GAS INJECTION

Massive gas injection is an extensively studied tool for disruption mitigation, including reduction of electro-mechanical and thermal loads as well as suppression of runaways [16, 17, 18, 19, 20, 21]. At JET, experiments with MGI have been performed since 2008 [6]. The gas injection is done by a fast disruption mitigation valve (DMV) situated at the top of the machine and connected to the vacuum vessel by a 4m long guiding tube [23]. The valve has a volume of 650ml and the maximum pressure is 3.6MPa. With CFC wall, various gases have been used: argon, neon, mixtures of those with 90% D₂ and helium. The injection of pure Ar and Ne led in many cases to the generation of runaway electrons. For the first campaigns with the new ILW, it was chosen to use only D₂ mixtures to avoid RE formation. The severe loads observed with the ILW, especially the heat loads during the current quench phase, made the use of MGI mandatory in pulses with plasma current of ≥ 2.5 MA. It is important to note that with the ILW no non-sustained breakdowns occurred after injection of D₂ mixtures in contrast to CFC wall. Severe impact of MGI on the performance of subsequent pulses has not been observed, however, a detailed analysis as has been done for CFC [22] is an open task.

4.1 MITIGATION EFFICIENCY

A high radiation fraction ranging between 70% and 100% of the plasma energy W_{plasma} is being radiated with MGI in both, CFC and ILW (see figure 4). Scatter in the data arises from the injected species and the injection time during disruptions. A significant difference in radiation fraction between CFC and ILW is not observed, but it is seen that MGI with ILW tends towards slightly higher current decay times (cf. figure 6). MGI reduces halo current and sideways impact by decreasing the current quench time, resulting in smaller vessel displacement (cf. figure 14). With the ILW, MGI can lead to higher amplitudes of the vessel rolling motion compared to CFC with the same halo current impulse. This is because of higher eddy current forces due to the very fast current quenches with MGI. The upward displacement related to the halo currents is virtually zero with MGI. Heat loads during the CQ are suppressed sufficiently because of the high radiation efficiency during the CQ and therefore low W_{cond} (cf. figure 15). Temperature measurements with IR cameras during MGI are disturbed by IR emission from inside the plasma. However, extrapolating the temperature decay on PFCs after the disruption shows that temperatures stay below 400°C.

The discussion of figure 4 refers to the efficiency of radiating both, magnetic and thermal energy. However, a high efficiency during the thermal quench is essential for ITER. In order to assess the efficiency of radiating the thermal energy a more detailed analysis has been done with the ILW by varying the fraction of thermal energy $W_{\text{th}}/W_{\text{tot}}$ using different NBI input power up to 18MW but also different plasma current. Figure 16 shows the radiation fraction for high injection rate (valve pressure about $p_{\text{DMV}} = 3.3\text{MPa}$), low injection rate ($p_{\text{DMV}} = 0.3\text{MPa}$) and for pure D_2 injection at high pressure. The radiation efficiency for pure D_2 is much lower compared to the $\text{Ar}+\text{D}_2$ mixture and also lower compared to D_2 with CFC wall, the latter showing that carbon contributed significantly to the total radiation. But also for the mixture, the radiation fraction drops from almost 100% for only ohmically heated pulses down to 70% at $W_{\text{th}}/W_{\text{tot}} \approx 0.5$. The drop is less severe for higher injection pressure. The decay in $W_{\text{rad}}/W_{\text{tot}}$ with increasing fraction of thermal energy indicates that mitigation is less efficient during the TQ. A linear fit gives a radiation efficiency in the TQ of only 50% for maximum injection rate. It is important to note, that the radiation is measured 90° toroidally away from the injection point. This has to be taken into account, as toroidal asymmetries are likely during MGI, especially in the pre-TQ and TQ phase. The measurements only represent the average radiated energy if asymmetries are negligible or if the toroidal distribution is such that the measurement position is giving the average radiation. It is therefore difficult to distinguish a drop in radiation efficiency from a variation in the toroidal distribution. Therefore, a second bolometer has been used to estimate the radiation at 135° from the injection point. Because both bolometers differ in geometry (see [24]) only a simplified estimate for the total radiated power could be used. However, both bolometers give the same trend with $W_{\text{th}}/W_{\text{tot}}$, which leads us to the conclusion that indeed a degradation of the radiation efficiency is taking place.

Control of the current quench time with MGI is important in order to minimise electromechanical loads. As described in section 3.1, a slow CQ leads to an increase of the impact of halo currents

whereas too fast a CQ will increase the loads caused by eddy currents. The latter limits the CQ times in ITER to values above 1.7ms/m^2 [25]. The current quench times with MGI in JET are more systematically analysed in figure 17, which shows the current decay time as function of the plasma current for a fixed amount of injected Ar/D₂ mixture for ILW and CFC. The current quench time shows an increase with plasma current as the amount of injected gas is kept constant, which is due to the increase in ohmic heating. This behaviour can be reproduced using the model described in section 2.3. The fit of the modelled curve to the data yields impurity densities $n_{\text{Ar/D}_2}$ of $2.3 \times 10^{20} \text{m}^{-3}$ for the ILW. The faster CQ with the CFC wall can be explained by adding 1% of carbon to the injected amount of Ar/D₂ (it is assumed that the fuelling efficiency remains unchanged) to account for carbon radiation that will add to the radiation from the injected gas. It is important to note, that the induced currents in the structure accelerate the current decay in the plasma. If not taken into account, impurity densities are overestimated. Extrapolation of existing data to ITER needs to take the dependence on plasma current into account. This is especially important in view of the ITER eddy current limit.

As reference, figure 17 also shows data for pure D₂ injection. The CQ time shows a remarkable difference between ILW and CFC. The CQ times for CFC are very close to the datapoints with Ar/D₂ injection, whereas for ILW τ_{CQ}/S is about a factor of 5 higher. Again, this is attributed to the carbon release during disruptions with CFC PFCs. The ILW data shows that D₂ might be a good candidate for increasing the density in the CQ without further accelerating the current decay. However, as density measurements are not available during MGI at JET, conclusions on the densification cannot be drawn here.

4.2 CLOSED LOOP OPERATION

The DMV is presently triggered by basic but robust disruption detection signals [26]. These are either the amplitude of a locked $n = 1$ mode or an excursion of the loop voltage, indicating the start of the CQ. The present system includes a longer delay caused by interlocks for the protection of heating sub-systems, which can be up to 50ms. Figure 18 shows an example of an actively mitigated disruption. The DMV was triggered by the mode-lock signal, which at the same time starts a soft stop sequence including reduction of plasma shaping and current. Injection takes place during the CQ as indicated by the drop in voltage in the DMV power supply (UPS,DMV), leading to a clear acceleration of the current decay, a stop of the upward displacement and consequently a low halo current fraction.

During the ILW campaigns 2011–2012 67 unintentional disruptions were mitigated by MGI. During the commissioning phase of the closed-loop operation, 5 disruptions were missed due to inhibits in the real-time protection system. Incorrect setting of the timing caused 4 missed disruptions. Taking human error and commissioning phase into account, the success rate is about 88%. Due to the type of trigger and due to the long interlock delay, all MGIs in closed-loop injected the gas after the first thermal quench. Mitigation was still successful with respect to CQ loads, because of

the slow current decay. However, the TQ has not been mitigated, which is only acceptable because the thermal energy dropped by that time to values typical for ohmic heating only. For the coming campaigns in 2013, the interlock delay will be shortened and new schemes for triggering have to be established to ensure also TQ mitigation.

SUMMARY, CONCLUSIONS & OUTLOOK

The use of beryllium for the first wall and tungsten in the divertor has shown a strong reduction of the radiation during disruptions compared to the previously installed CFC wall. This results in slower current quench rates and consequently in higher halo current and sideways impact as well as in high heat loads at still moderate stored energies. For ITER this means that heat loads need to be considered also for the current quench. They affect first wall structures and might be an issue already at still low input power but high current. High radiation fractions can be regained by MGI, which is essential to protect the ILW from melting. However, although the mitigation efficiency with respect to heat loads is easily sufficient for JET, the low radiation efficiency during the TQ is worrying and far from the ITER requirements of 90% radiation fraction. A second DMV is planned to be installed in JET in 2013 at the outer midplane. This will give the opportunity to study the impact of multiple injection and injection location on mitigation efficiency. Dedicated experiments are also planned for further understanding the impact of the ILW on runaway electron generation and for testing massive gas injection for runaway electron mitigation.

ACKNOWLEDGEMENTS

This work was supported by EURATOM and carried out within the framework of the European Fusion Development Agreement. The views and opinions expressed herein do not necessarily reflect those of the European Commission.

6. APPENDIX

A HALO CURRENT MODEL

The halo current model used in section 3.1 is based on the same principles as described in [11]. Three quantities are determined by the model, the plasma vertical position given as distance between plasma center and first wall $Z(t)$, the plasma core current density $j(t)$ and the current in the halo $I_H(t)$. We consider only post-TQ VDEs although the model could be applied to pre-TQ VDEs as well. The vertical position develops exponentially in time away from the equilibrium position Z_{eq} after an initial offset δ_Z which occurs during the TQ. When $Z \leq \kappa a_p$ the plasma is limited by the first wall and the vertical velocity is considered to be constant:

$$\frac{d}{dt}Z = \begin{cases} -\gamma_{Z,lin} \kappa a_p & : Z < \kappa a_p \\ -\gamma_{Z,exp}(Z - Z_0) & : Z \geq \kappa a_p \end{cases}, \quad (5)$$

with initial plasma radius a_p and elongation κ . The decay rates in both phases are related to each

other: $\gamma_{Z,\text{lin}} = \gamma_{Z,\text{exp}} \Delta_{\text{gap}} \kappa^{-1} a_p^{-1}$, with Δ_{gap} being the gap between separatrix and upper first wall during equilibrium. The vertical position at time $t = 0$ is $Z_0 = \kappa a_p + \Delta_{\text{gap}} - \delta_Z = Z_{\text{eq}} - \delta_Z$. The plasma cross section area A develops as follows:

$$A = \begin{cases} \pi Z^2 / \kappa & : Z < \kappa a_p \\ \pi \kappa a_p^2 & : Z \geq \kappa a_p \end{cases} . \quad (6)$$

The core plasma current density is determined by the ohmic resistance and by transfer of core current into the halo region during shrinking of the plasma cross section:

$$\frac{d}{dt} j = -\gamma_P j , \quad (7)$$

with $\gamma_P = R_{\Omega,P} / L_P$ and plasma resistance $R_{\Omega,P}$ and inductance L_P . The halo current is given by [11]

$$\frac{d}{dt} I_{H,\text{tor}} = -\gamma_H I_{H,\text{tor}} - \left(1 + \frac{1}{2\Gamma_H} \right) \frac{d}{dt} (Aj) , \quad (8)$$

with δ_H being the resistive decay rate in the halo and $\Gamma_H = \log(8R_P / a_P \sqrt{k}) - 2$. We link the decay rate in the halo with the decay rate of the core by the ratio of the cross-sectional areas:

$$\gamma_H = \gamma_P \frac{1}{(1 + \delta_H / a_P)^2 - 1} , \quad (9)$$

with halo width δ_H . This relation reflects the assumption that the resistivity in both, plasma core and halo, is the same. It is an approximation as different inductances in the plasma core and the halo are not taken into account. The poloidal halo current $I_{H,\text{pol}}$ is related to the toroidal halo current by the safety factor in the halo region $I_{H,\text{pol}} = I_{H,\text{tor}} / q_H$. The safety factor q_H is taken as an "average" value:

$$q_H = q_0 \left(\frac{\sqrt{A/\pi} + \delta_H/2}{a_P + \delta_H/2} \right)^2 \frac{I_P^0}{(Aj + I_{H,\text{tor}}/2)} , \quad (10)$$

with the restriction $q_H \geq 1$.

Important to note is that the measured plasma current includes all currents inside the vacuum vessel as measured by the fractional Rogowski loop and therefore also a large fraction of the toroidal halo current. When comparing the model results to the measurements, we take this into account:

$$I_{P,\text{measured}} = I_P + I_{H,\text{tor}} \left(1 - \frac{A_{\text{secant}}}{\pi a_P^2 - A} \right) \quad (11)$$

with

$$A_{\text{secant}} = a_P^2 \arcsin\left(\sqrt{1 - \frac{A}{\pi a_P^2}}\right) - \sqrt{\frac{A a_P^2}{\pi} - \frac{A^2}{\pi^2}} . \quad (12)$$

REFERENCES

- [1]. Sugihara M et al., 24th IAEA Fusion Energy Conference, San Diego, USA (2012) ITR/P1-14.
- [2]. Matthews G F et al., Journal of Nuclear Materials (2013) <http://dx.doi.org/10.1016/j.jnucmat.2013.01.282>.
- [3]. de Vries P.C et al., Plasma Physics and Controlled Fusion **54** (2012) 124032.
- [4]. Huber A et al., Journal of Nuclear Materials (2013) <http://dx.doi.org/10.1016/j.jnucmat.2013.01.022>.
- [5]. Riccardo V et al., Plasma Physics and Controlled Fusion **44** (2002) 905.
- [6]. Lehnen M et al., Nuclear Fusion **51** (2011) 123010.
- [7]. Lehnen M et al., Journal of Nuclear Materials (2013) <http://dx.doi.org/10.1016/j.jnucmat.2013.01.016>.
- [8]. Giovannozzi E et al., Review of Scientific Instruments **81** (2010) 10E131.
- [9]. Wesley J C et al., Proceedings of the 21th IAEA Fusion Energy Conference, Chengdu, China (2006) IT/P1-21.
- [10]. Gerasimov S.N et al., 39th EPS Conference on Plasma Physics Stockholm, July 2 - 6, ECA 36F, P-5.074 (2012)
- [11]. Humphreys D.A and Kellman A.G, Physics of Plasmas **6** (1999) 2742.
- [12]. Plyusnin V.V et al., 24th IAEA Fusion Energy Conference, San Diego, USA (2012) EX/P8-05.
- [13]. Lehnen M et al., Journal of Nuclear Materials **390-391** (2009) 740.
- [14]. Helander P et al., Plasma Physics and Controlled Fusion **44** (2002) B247.
- [15]. Harris G.R., Comparison of the current decay during carbon-bounded and beryllium-bounded disruptions in JET, JET Joint Undertaking Report (1990) JET-R(90)07.
- [16]. Hollmann E.M et al., Nuclear Fusion **45** (2005) 1046.
- [17]. Granetz R.S et al., Nuclear Fusion **47** (2007) 1086.
- [18]. Pautasso G et al, Plasma Physics and Controlled Fusion **51** (2009) 124056.
- [19]. Reux C et al., Nuclear Fusion **50** (2010) 095006.
- [20]. Bozhenkov S.A et al., Nuclear Fusion **51** (2011) 083033.
- [21]. Thornton A.J et al., Plasma Physics and Controlled Fusion **54** (2012) 125007.
- [22]. Kruezi U et al., Journal of Nuclear Materials **415** (2011) S828.
- [23]. Kruezi U et al., 36th EPS Conference on Plasma Phys. Sofia, June 29 - July 3, ECA 33E, P-2.153 (2009).
- [24]. Huber A et al., Fusion Engineering and Design **82** (2007) 1327.
- [25]. Hender T.C et al., Nuclear Fusion **47** (2007) S128.
- [26]. Reux C et al., Fusion Engineering and Design (2013) <http://dx.doi.org/10.1016/j.fusengdes.2012.12.026>.

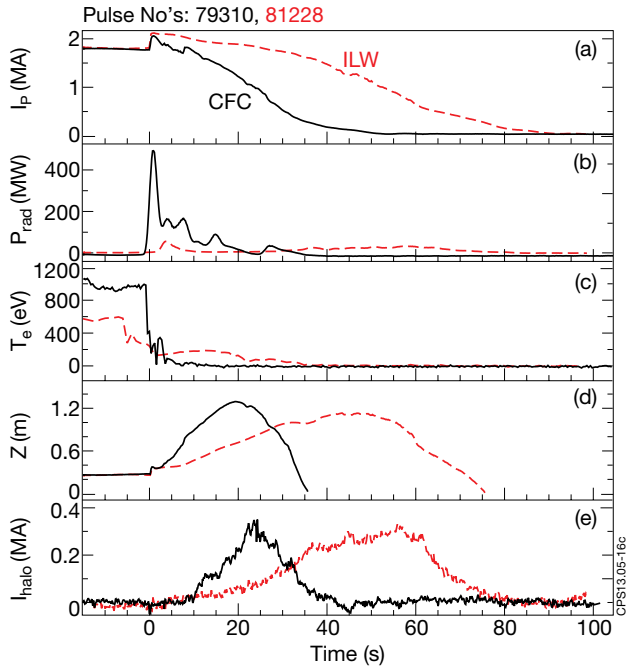


Figure 1: Comparison of two high triangularity ($\langle\delta\rangle \approx 0.42$) disruptions with CFC and ILW, which reflect the typical changes with introduction of a metallic wall: a) plasma current, b) total radiated power, c) central electron temperature, d) vertical plasma position, e) poloidal halo current.

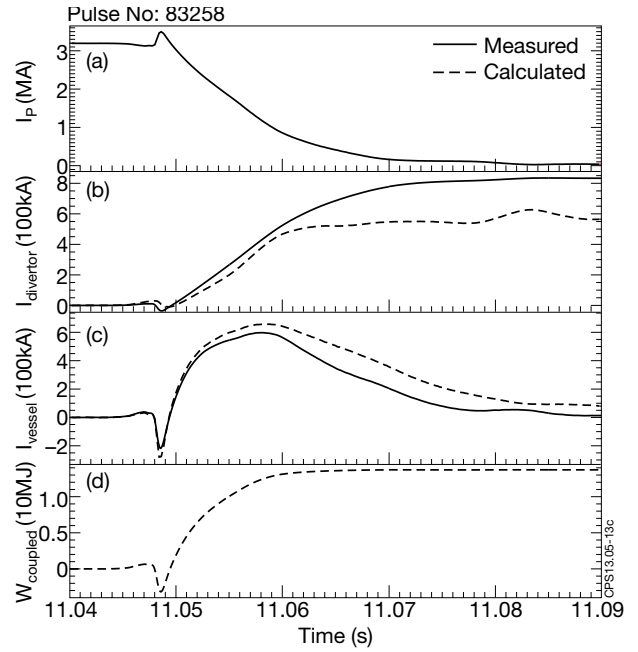


Figure 2: Example of the calculated current in the structure for a MGI disruption: a) plasma current, b) divertor current, c) current in the vacuum vessel, d) cumulative integral of the energy coupled to the structure.

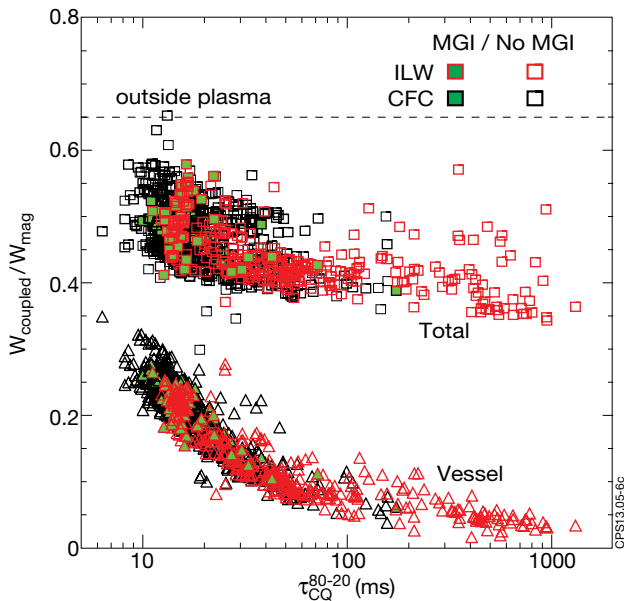


Figure 3: Fraction of energy coupled into poloidal field coils and vacuum vessel. The current quench time is the linear extrapolation of the current drop from 80% to 20% of the pre-TQ current. The dashed line indicates the fraction of magnetic energy residing outside the vacuum vessel.

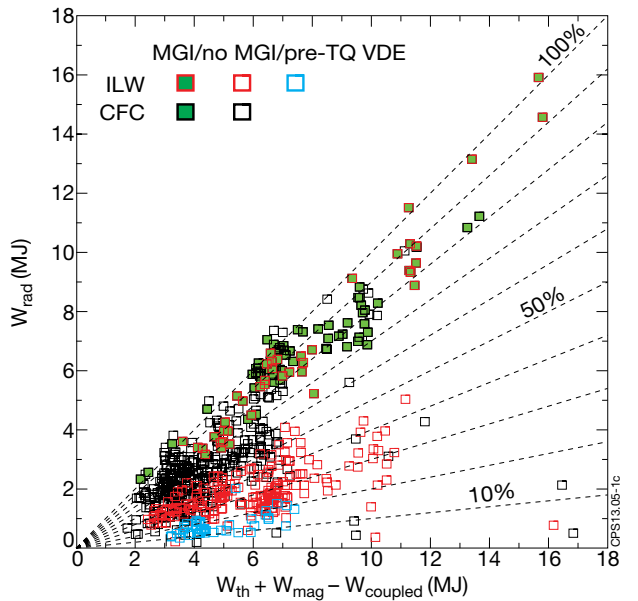


Figure 4: Radiated energy as function of the energy available in the plasma.

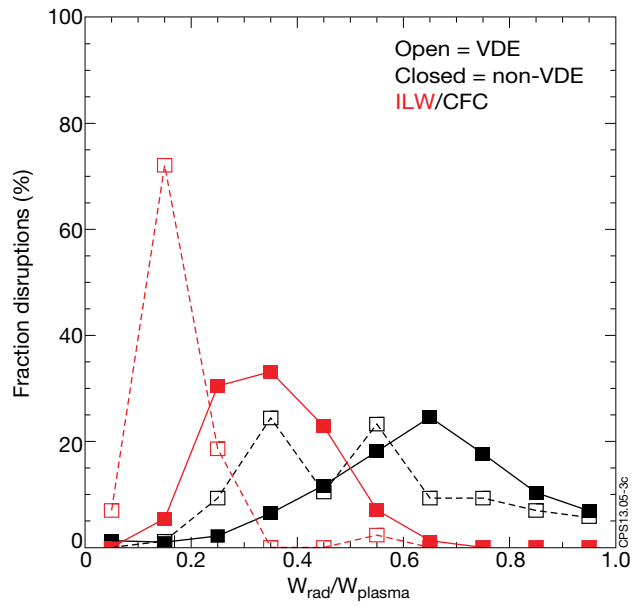


Figure 5: Distribution of the fraction of radiated energy.

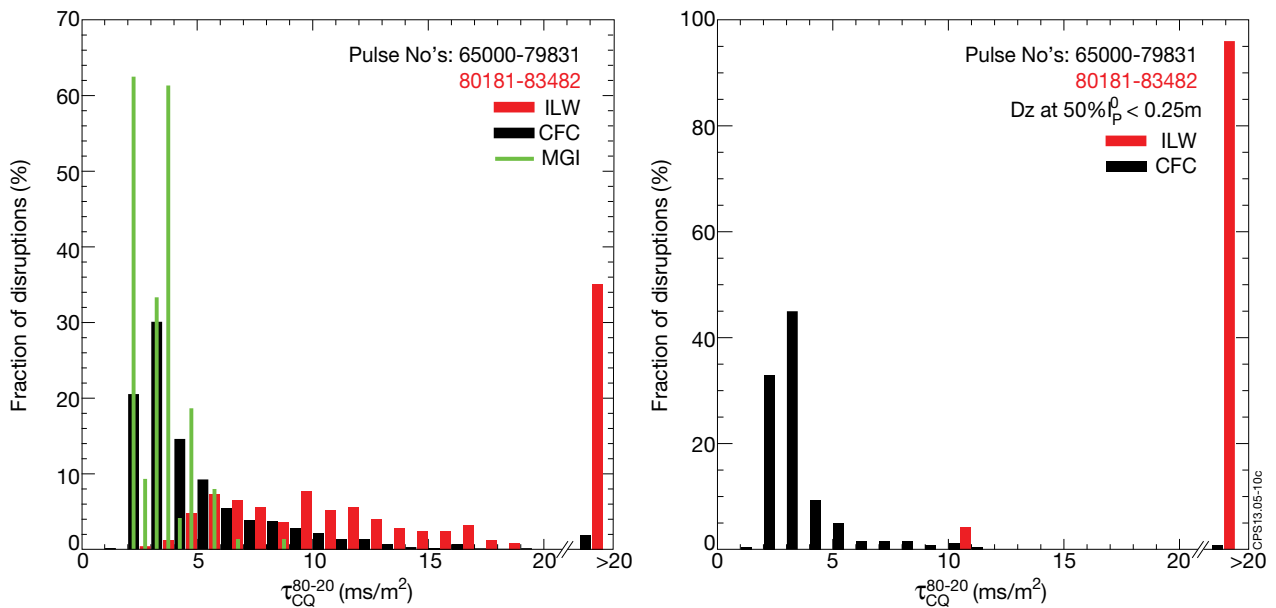


Figure 6: Current quench times: a) all disruptions except for disruptions with runaways, b) disruptions with vertical movement below 0.25m for $I_p > 0.5 \times I_p^0$.

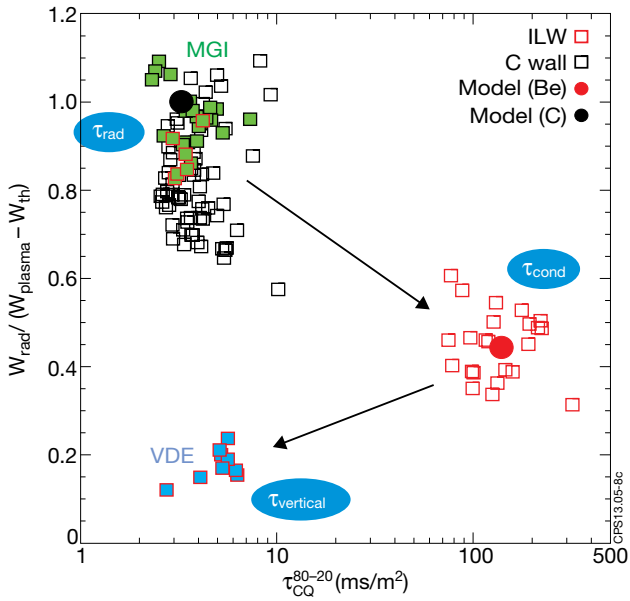


Figure 7: Radiated energy as function of the linear current quench time. Open symbols and green closed symbols (MGI): vertical displacement below 0.25 m at 50% of the initial plasma current. Blue closed symbols for pre-TQ VDEs (deliberately displaced before the thermal quench). MGI data is showing $W_{\text{rad}}/W_{\text{plasma}}$ as thermal energy is radiated as well in this case.

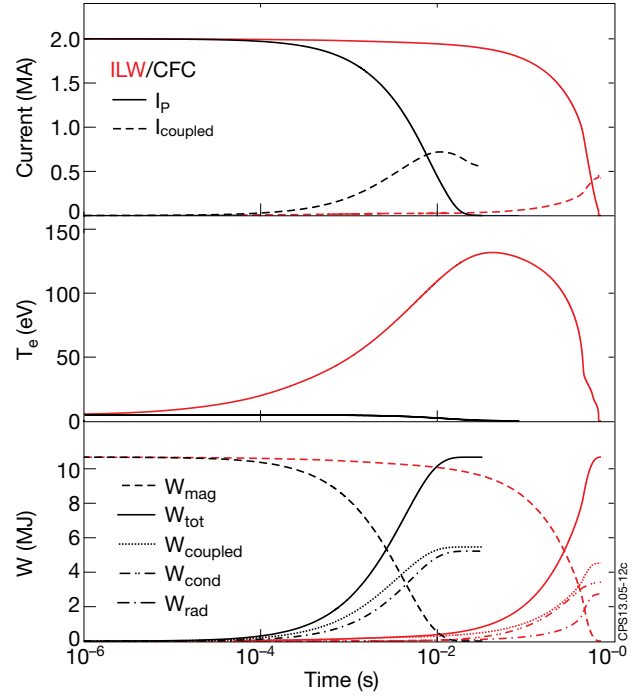


Figure 8: Timetraces for the current quench model described in eqs. 2 and 3. The impurity density is $n_Z = 7 \times 10^{18} \text{ m}^{-3}$ with carbon injection for CFC and Be injection for ILW. The thermal energy loss time is $\tau_{\text{cond}} = 30 \text{ ms}$. Note that the time axis is on logarithmic scale.

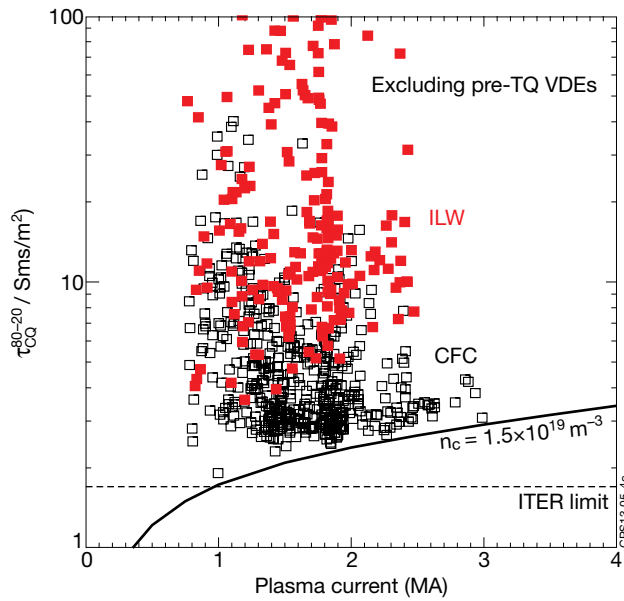


Figure 9: Linear current quench times extrapolated from 80% to 20% decay as function of plasma current. The solid black line is the calculated decay time for a carbon density of $n_C = 1.5 \times 10^{19} \text{ m}^{-3}$ and internal inductance of $l_i = 1.0$ (see section 2.3). The dashed line indicates the lower limit for CQ times in ITER given by the maximum acceptable forces from eddy currents [25].

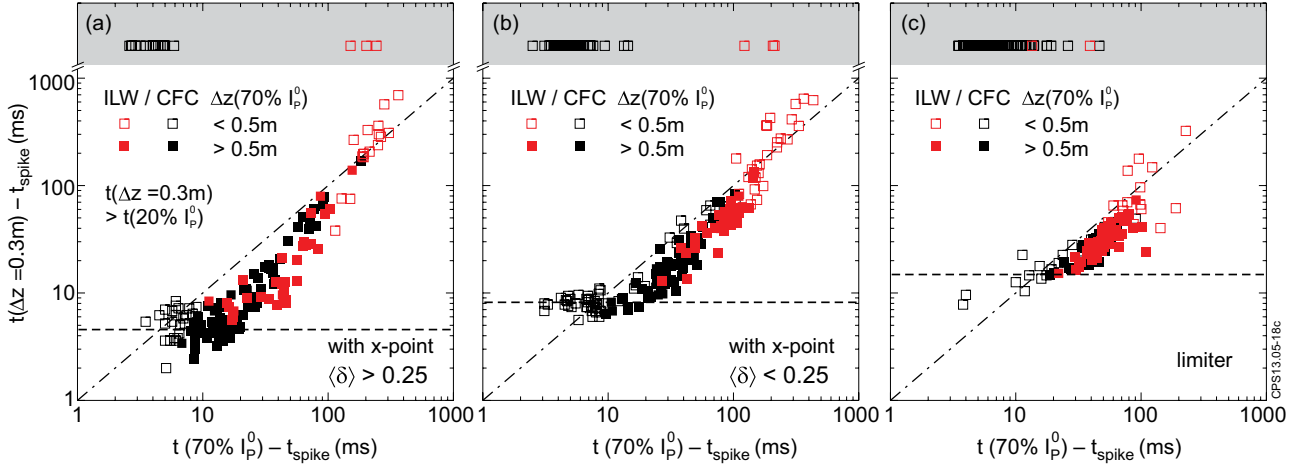


Figure 10: Vertical growth time in the early phase of the disruption versus the current decay time down to $70\% I_p^0$ for a) high and b) low triangularity with x-point and for c) limiter configuration.

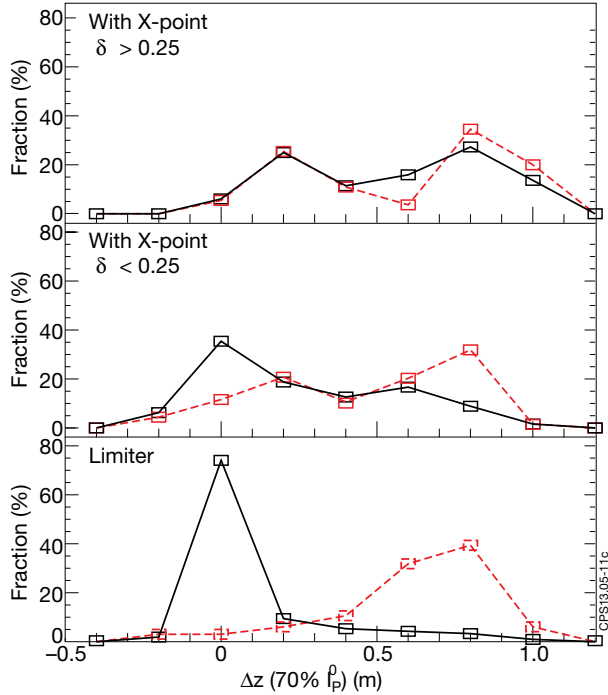


Figure 11: Probability distribution for the displacement of the plasma column at $70\% I_p^0$.

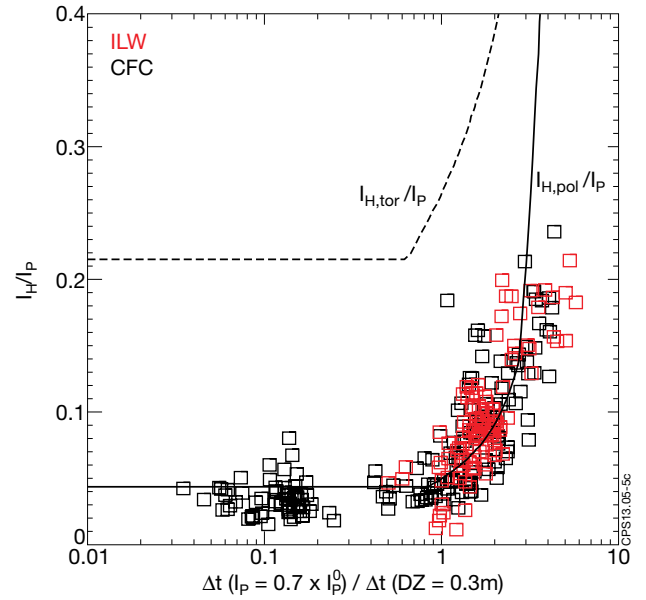


Figure 12: Halo current fraction as function of the ratio between the time for a current decay to $70\% I_P^0$ and the time for a displacement of $\Delta Z = 0.3\text{m}$. Dashed line is the maximum toroidal halo current fraction as derived from the halo current model and the solid line is the poloidal halo current fraction (see Appendix A). The model parameters are $\Delta_{\text{gap}} = 0.2\text{m}$, $\Delta Z = 0.1\text{m}$, $\kappa = 1.6$, $a_p = 1.0\text{m}$, $\delta_H = 0.1\text{m}$, $R_p = 2.9\text{m}$.

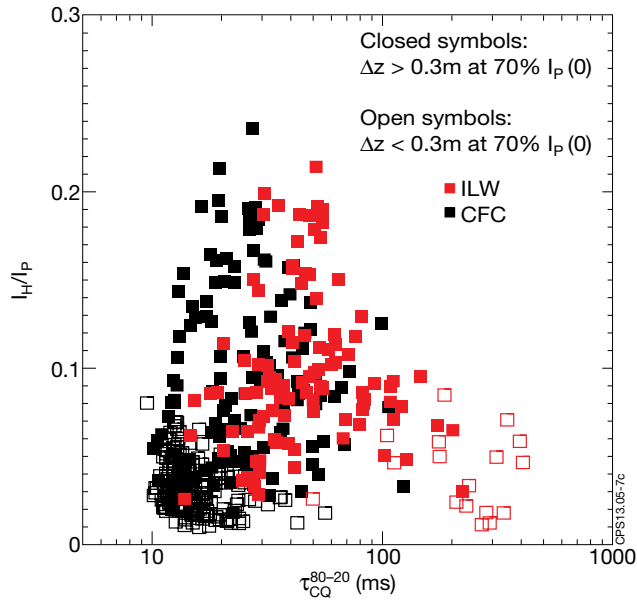


Figure 13: Halo current fraction as function of the linear current quench time excluding pre-TQ VDEs.

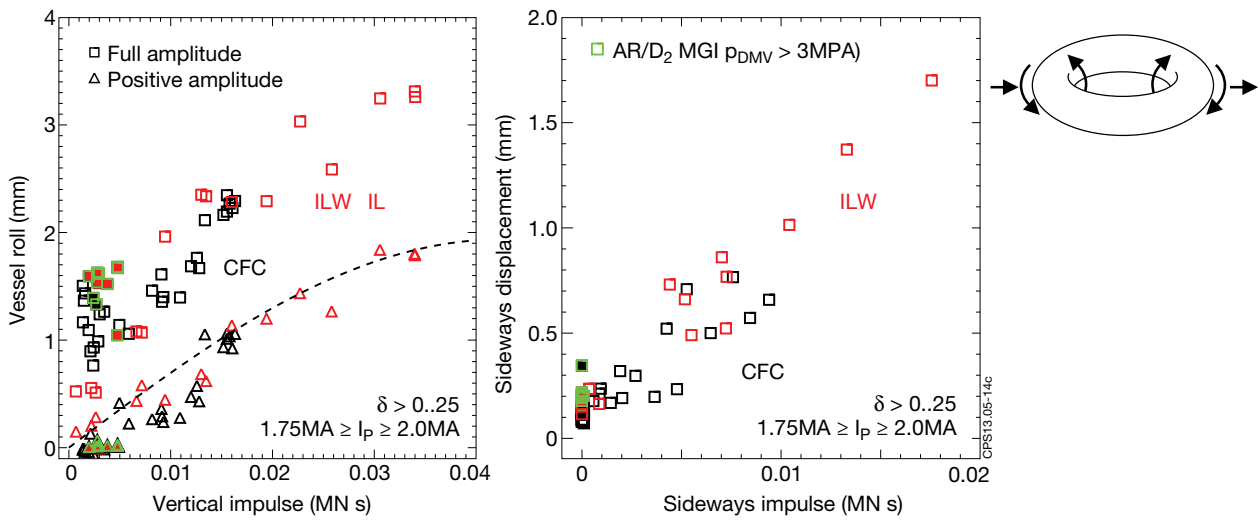


Figure 14: Vessel rolling amplitude and sideways displacement as function of vertical and sideways impulse. All data for $1.75\text{MA} < I_p < 2.0\text{MA}$ and $\langle \delta \rangle > 0.25$. The dashed line refers to a spring-mass system with maximum applied force of 1.2MN (corresponding to $B_t = 3T$, $I_p = 2\text{MA}$ and $I_H/I_P = 0.2$), a mass of 160t and resonant frequency of 14Hz .

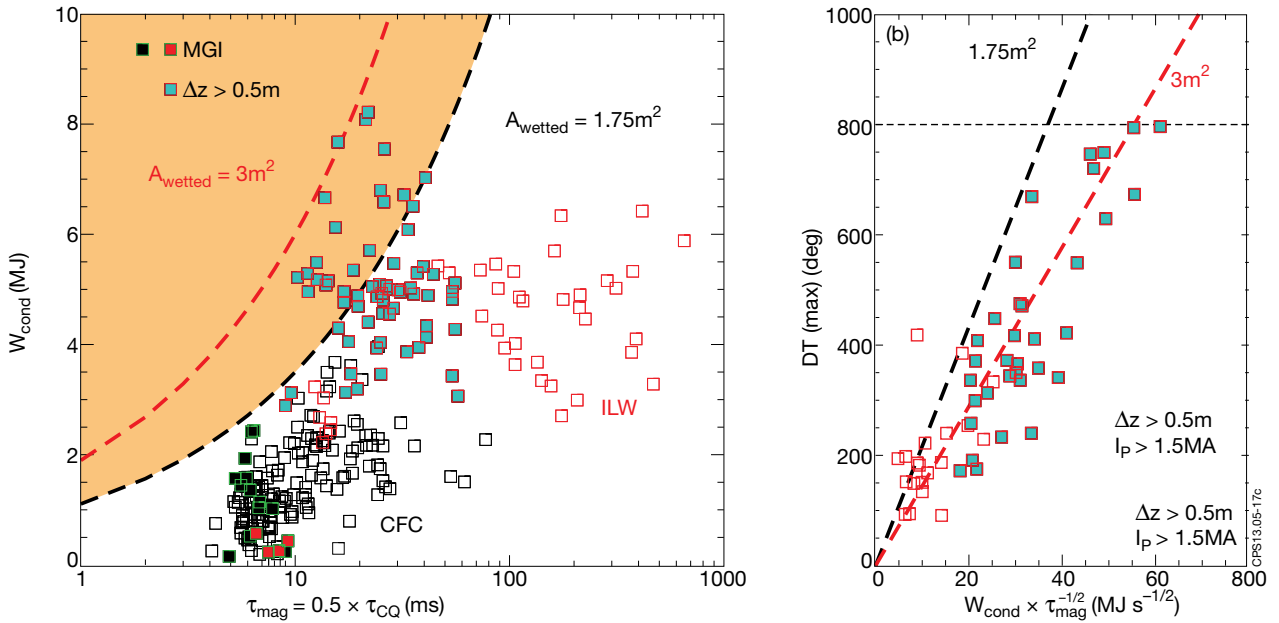


Figure 15: Heat load for disruptions with $W_{\text{th}}/W_{\text{mag}} < 0.1$. a) Energy that is conducted/ convected during the disruption as function of the loss time of the magnetic energy ($\tau_{\text{mag}} = \tau_{\text{CQ}}/2$). Dashed lines indicate the melting limit for Be of $25\text{MJm}^{-2}\text{s}^{-1/2}$. b) Maximum temperature rise on upper inner wall protection limiter and dump plate during the disruption.

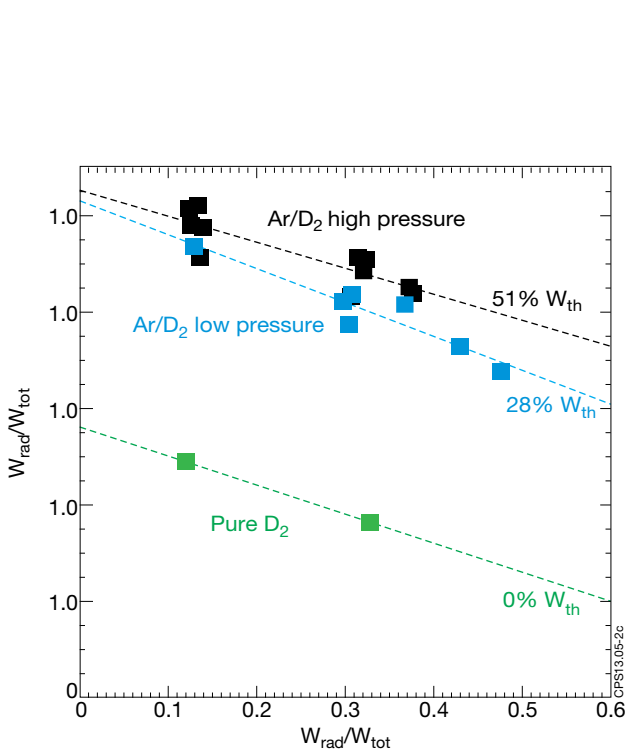


Figure 16: Radiated energy during MGI as function of the fraction of thermal energy stored in the plasma before injection.

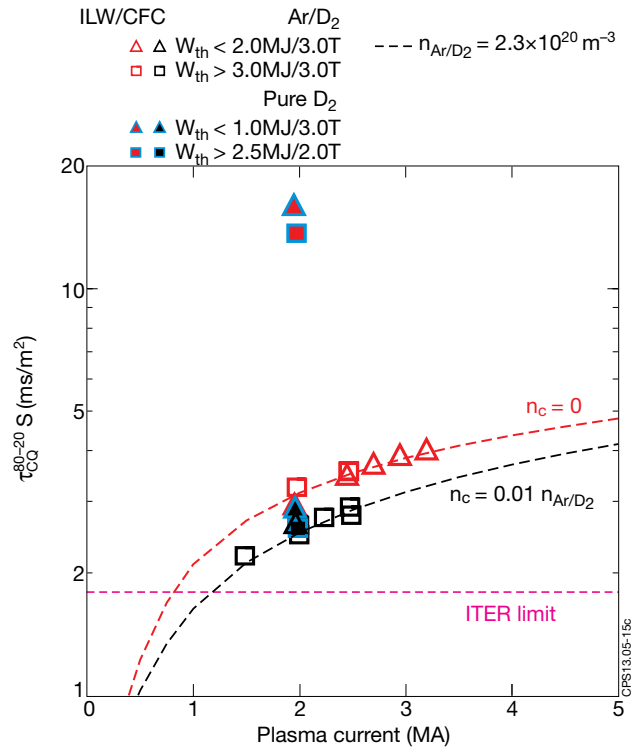


Figure 17: Linear current quench time versus plasma current. The dashed lines are from the current quench model with $n_{\text{Ar}/\text{D}_2} = 2.3 \times 10^{20} \text{m}^{-3}$. For CFC 1% of carbon has been added to fit the experimental data with the same amount of Ar/D₂ gas. Internal inductance is set $l_i = 1$.

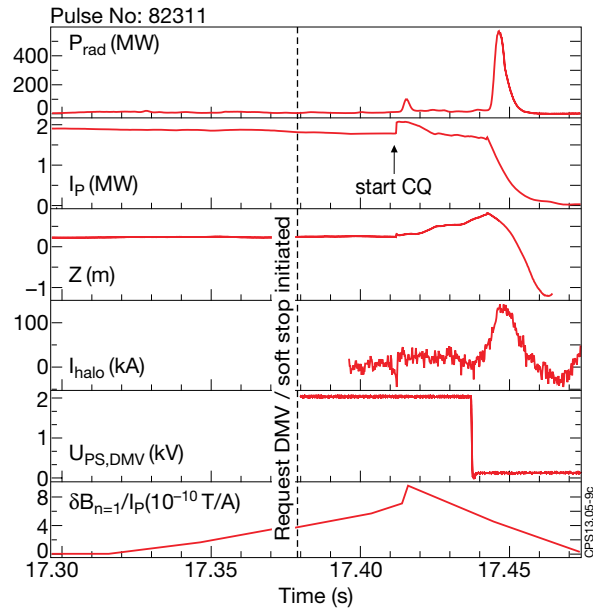


Figure 18: Example of closed loop operation of the DMV with $p_{DMV} = 3.2\text{MPa}$ and Ar + D₂ injection.